WILEY-VCH

Nucleation Regulation and Mesoscopic Dielectric Screening in α-$FAPbI_3$

Ruijia Tian[a,b], Chang Liu[a]*, Yuanyuan Meng[a], Yaohua Wang[a], Ruikun Cao[a], Bencan Tang[b], Darren Walsh[d], Hainam Do[b], Haodong Wu[e], Kai Wang[e]*, Kexuan Sun[a], Shuncheng Yang[a], Jintao Zhu[b], Xin Li[a], Ziyi Ge[a,c]*

[a]Zhejiang Provincial Engineering Research Center of Energy Optoelectronic Materials and Devices, Ningbo Institute of Materials Technology & Engineering, Chinese Academy of Sciences, Ningbo 315201, China

[b]Department of Chemical and Environmental Engineering, University of Nottingham Ningbo China, Ningbo 315100, China

[c]Center of Materials Science and Optoelectronics Engineering University of Chinese Academy of Sciences, Beijing 100049, China

[d]Carbon Neutral Laboratory for Sustainable Chemistry, Innovation Park, Triumph Road, Nottingham NG7 2TU, UK

[e]Department of Materials Science and Engineering, Pennsylvania State University, University Park, PA, 16802 USA

*Corresponding authors E-mail: liuchang1@nimte.ac.cn; kaiwang@psu.edu; geziyi@nimte.ac.cn.

Keywords: Polarity engineering; nucleation regulation; dielectric screening; nonradiative decay; perovskite solar modules.

Abstract

While significant advancements in power conversion efficiencies (PCEs) of α-$FAPbI_3$ perovskite solar cells (PSCs) have been made, attaining controllable perovskite crystallization is still a considerable hurdle. This challenge stems from the initial formation of δ-$FAPbI_3$, a more energetically stable phase than the desired black α-phase, during film deposition. This disrupts the heterogeneous nucleation of α-$FAPbI_3$, causing the formation of mixed phases and defects. To this end, we introduced polarity engineering using molecular additives, specifically (methyl-sulfonyl)phenyl)ethylamines (MSPEs). Our findings reveal that the interaction of PbI_2-MSPEs-FAI intermediates is enhanced with the increased polarity of MSPEs, which in turn expedites the nucleation of α-$FAPbI_3$. This leads to the development of high-quality α-$FAPbI_3$ films, characterized by vertical crystal orientation and reduced residual stresses. Additionally, the increased dipole moment of MSPE at perovskite grain boundaries attenuates Coulomb attractions among charged defects and screens carrier capture process, thereby diminishing non-radiative recombination. Utilizing these mechanisms, PSCs treated with highly polar 2-(4-MSPE) achieve an impressive PCE of 25.2% in small-area devices and 20.5% in large-area perovskite solar modules (PSMs) with an active area of 70 cm^2. These results demonstrate the effectiveness of this strategy in achieving controllable crystallization of α-$FAPbI_3$, paving the way for scalable-production of high-efficiency PSMs.

1. Introduction

Formamidinium lead triiodide ($FAPbI_3$), exhibiting impressive optoelectronic properties, ideal bandgap, and remarkable thermal resistance, has emerged as a prominent contender in developing high-performance perovskite solar cells (PSCs). [1–6] The $FAPbI_3$ active absorber has been found to achieve the most state-of-the-art PSCs, with certified power conversion efficiencies exceeding 26%[7], which outperforms devices based on other perovskite systems. However, the thermodynamically stable δ-$FAPbI_3$ is easily formed under room temperature prior to the photoactive α-$FAPbI_3$, which disrupts the rapid nucleation of the α-phase and hinders complete coverage of the polycrystalline film.[8,9] Additionally, there is a reversible transition between the α-phase and the δ-phase that occurs spontaneously under room temperature, resulting from a significant lattice distortion. This transition restricts the long-term stability of PSCs.[10] Therefore, despite the great progress in small area PSCs, achieving controllable crystallization for large area and stable α-$FAPbI_3$ perovskite films remains a major challenge.

Several techniques have been used to tune the perovskite crystallization process and stabilize the α-black phase of $FAPbI_3$, one of the most effective being the formation of adducts with $[PbI_6]^{4-}$ inorganic octahedral and hydrogen bonds with FAI. For instance, Huang et al. adopted ionic liquid methylamine formate (MAFa) to mediate Pb-I cluster structure through the formation of C=O···Pb chelation and N-H···I bond, which was observed to promote the vertical growth of perovskite crystals relative to substrate.[9] PbI_2·NMP-templated crystallization of FA-based perovskite also enabled a high PCE of 23% for small-area PSCs and over 20% for 17.1 cm^2 solar modules.[11] Recently, Zhao et al. further introduced 1-butylpyridine tetrafluoroborate ($BPyBF_4$) additive into perovskite precursor to realize a spontaneous formation of α-$FAPbI_3$ with high uniformity, resulting in an outstanding PCE of 21.6% for solar module with an active area of 10 cm^2.[12] The aforementioned findings establish the practicability of this technique in producing perovskite films on large scale. It is noted that the nucleation and crystallization steps, being affected by the formation energy of perovskite nuclei, are strongly dependent on the strengths of C=O···Pb chelation and N-H···I bond.[13] However, a thorough investigation of the aforementioned correlations and the underlying mechanisms of the film formation process remain obscure, which in turn inhibits the rational design and screening of more efficient functional additives.

Aside from affecting the film formation and phase stability of α-$FAPbI_3$, severe lattice distortion of the $[PbI_6]^{4-}$ octahedron easily causes the creation of antisite defect pairs (Pb_I and I_{Pb}) or interstitial defects (Pb_i).[14] The Coulomb interaction between the negatively charged and positively charged defect sites has been pinpointed as the primary cause of carrier capture losses, resulting in the nonradiative recombination of PSC devices.[15] However, majority of the present researches solely concentrate on passivating trap states chemically, disregarding the significance of minimizing carrier capture losses. Independently, Liu and Zhu et al. indicated that the incorporation of substances with high dipole moment and polarization could act as dielectric screen to Coulomb attractions between defect sites, thus diminishing the probability of carrier capture.[16,17]

Herein, a series of multifunctional additives (methyl-sulfonyl)phenyl)ethylamine (MSPEs, as shown in Figure 1a and Figure S1) have been designed, showcasing a pioneering approach in manipulating the α-$FAPbI_3$ nucleation and crystallization processes through precise

control of additive polarity. The MSPEs feature highly polar sulfonyl groups that form strong coordination with PbI_2, while the ethylamine groups establish hydrogen bonds with FAI,[18,19]facilitate a 'dual-site regulation' approach. This novel methodology goes beyond traditional coordination dynamics between PbI_2 and additives, allowing us to fine-tune the strength of not only O=S=O···Pb chelation, but also N-H···I bonding between perovskite and additives. The dipole moment of the MSPE series molecules could be facilely regulated by changing the relative substitution sites (para-, ortho-, and meta-) of the electron-donating ethylamine and electronegative sulfonyl group, which also enables the strength regulation of O=S=O···Pb chelation and N-H···I bond between MSPEs with perovskite. It thus allows for the in-depth investigation of perovskite crystallization induced by PbI_2-MSPEs-FAI intermediates. By real-time monitoring of the perovskite film formation process through in-situ optical spectroscopy measurements, we have found that stronger chelation and hydrogen bonding interactions lead to faster α-$FAPbI_3$ nucleation without the contribution of the yellow δ-phase, resulting in enhanced polycrystalline film crystallization with larger grain size, preferred (100) orientation and reduced residual tensile stress. Furthermore, the substitution of the para-site with 2-(4-MSPE) results in the largest dipole moment, granting the perovskite grains a dielectric atmosphere that efficiently shields the electron capture pathways and diminishes nonradiative recombination losses in the device. As a result, the PSCs based on the most polarizable 2-(4-MSPE) additive deliver an impressive PCE of 25.2%, The device exhibits significantly enhanced ambient and operational stability, attributable to the release of residual stresses in the film. This novel approach of molecular polarity modulation enables controllable perovskite nucleation and crystallization, culminating in homogenously deposited large-area perovskite solar modules (PSMs) (active area 70 cm^2) with an exceptional PCE of 20.5%. This efficiency is among the highest reported for solar modules of this scale.[7,20,21] Our results provide theoretical guidance for the systematic development of chemical additives to substantially improve the effectiveness and productivity of PSMs.

2. Results and Discussion

Molecules with different polarities are designed by attaching electron-donating ethylamine group and electron-withdrawing sulfonyl group on different substitution sites of the benzene ring. According to the electrostatic potential (ESP) calculations shown in Figure 1a, the dipole moments of the para- (2-(4-MSPE)), meta- (2-(3-MSPE)) and ortho-substitution (2-(2-MSPE)) show a successive decrement from 4.99, 4.03 to 3.63 Debye. To study the dependence of the strengths of MSPE-$FAPbI_3$ interactions on molecular polarity, the theoretical adsorption energy of MSPE on $FAPbI_3$ was firstly calculated. From Figure 1b-d, additive with the highest dipole moment (2-(4-MSPE)) exhibits more negative adsorption energy of -0.90 eV than that of 2-(2-MSPE) (-0.58 eV) and 2-(3-MSPE) (-0.35 eV), suggesting the strongest interaction between $FAPbI_3$ and 2-(4-MSPE). The Electron Localization Functions (ELFs), presented as 2D mappings in Figure S2, were calculated for the three adsorption models based on their optimized structures. The results reveal distinct ELF distributions: 2-(3-MSPE) and 2-(2-MSPE) demonstrate high ELF values around hydrogen (H) atoms, while 2-(4-MSPE) exhibits elevated ELF values in the vicinity of iodine (I) atoms. This indicates that in the 2-(4-MSPE)-$FAPbI_3$ structure, stronger hydrogen bonds are likely to form. The rationale behind this is that the electron-rich iodine atoms in 2-(4-MSPE) have a greater capacity to donate electrons,

thereby enhancing the stability of the hydrogen bonds formed in the structure. In addition, observations from the cross-sectional diagrams of electron density distribution (Figure S3) reveal a noticeable charge accumulation between the sulfonyl groups of MSPE and Pb at the perovskite surface. Notably, in the case of 2-(4-MSPE), the sulfonyl group exhibits the most pronounced electron accumulation, indicating a stronger and more stable adsorption to perovskite compared to the other MSPEs.

To further verify the hydrogen bonding and chelation between MSPEs and perovskite, Fourier transform infrared (FTIR) spectroscopy measurements were then implemented. From FTIR results in Figure 1e-g, the peaks around 1645 cm^{-1} in MSPE molecules, which are assigned to the scissoring vibration peaks of amino group $\delta(NH_2)$, shift to lower wavenumbers of 1634 cm^{-1} and 1620 cm^{-1} with FAI addition, for 2-(2-MSPE) and 2-(3-MSPE), respectively, and even disappear for 2-(4-MSPE). It reveals the greatly weakened N-H bond in MSPEs with the addition of FAI.[19] This might be caused by the N-H···I formed between MSPE and FAI, the strength of which increases with the molecular polarity (2-(4-MSPE)>2-(3-MSPE)>2-(2-MSPE)). Similarly, the sulfonyl group stretching vibration peaks ν(S=O) of the MSPEs around 970 cm^{-1} show blue-shift by 14 cm^{-1}, 10 cm^{-1}, and 5 cm^{-1} with PbI_2 addition, for 2-(4-MSPE), 2-(3-MSPE) and 2-(2-MSPE), respectively. This confirms the O=S=O···Pb chelation formed between MSPEs and PbI_2, the strength also intensifies with the molecular polarity. X-ray photoelectron spectroscopy (XPS) of perovskite films with and without additives were also studied. It is observed from Figure 1h that XPS peaks appear at 168 eV and 162 eV with the addition of MSPE additives, which are assigned to S $2p_{1/2}$ and S $2p_{3/2}$ from the sulfonyl group. From Figure 1i-j, Pb 4f signals (Pb $4f_{5/2}$ at 143 eV and Pb $4f_{7/2}$ at 138 eV) and I 3d signals (I $3d_{3/2}$ at 630 eV and I $3d_{5/2}$ at 619 eV) all shift to lower binding energies with MSPEs addition, following the same shift trend with molecular dipole moment. It further confirms the N-H···I bonding and O=S=O···Pb coordination formed between MSPEs and perovskite, which could also serve as chemical passivation for the uncoordinated Pb^{2+} and halide vacancies.

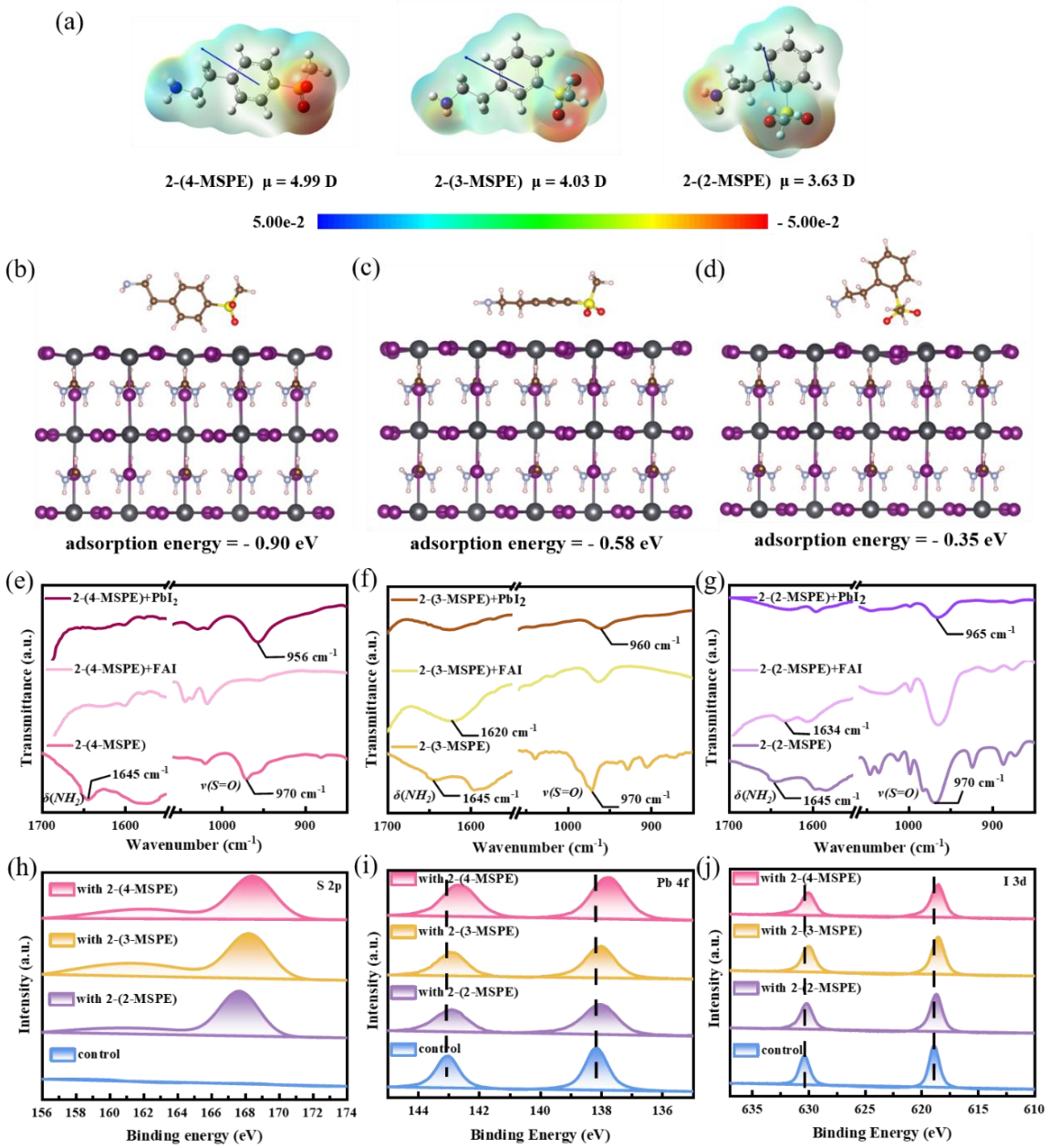

Figure 1. (a) The distribution of electrostatic potential (ESP) and dipole moments (μ) of MSPEs. Theoretical absorption energy between $FAPbI_3$ perovskite and (b) 2-(4-MSPE), (c) 2-(3-MSPE), and (d) 2-(2-MSPE). Fourier Transform Infrared (FTIR) spectra of (e) 2-(4-MSPE), (f) 2-(3-MSPE), and (g) 2-(2-MSPE), and their mixture with perovskite precursors (FAI and PbI_2). X-ray photoelectron spectra (XPS) of (h) S *2p*, (i) Pb *4f*, and (j) I *3d* of corresponding perovskite films.

The effects of molecular polarities on the film formation process of α-$FAPbI_3$ were explored by in-situ UV-vis absorption spectroscopy. It is worth to note that all the films used for characterizations were based on additives with the optimal concentration of 0.19 mg/mL according to photovoltaic performance optimization described in later context. Figure 2a-d illustrate the real-time monitoring of the perovskite nucleation and crystallization during spin-coating and thermal annealing, Figure 2e,f show their corresponding absorption peak positions, and Figure S4a,b display their corresponding absorption peak intensities. From Figure 2a,c, it can be observed that there are two main differences between pristine and 2-(4-MSPE)-treated perovskite during the spin-coating process. Firstly, during the solvent volatilization period with

an absorption peak around ~400-450 nm, which is assigned to the crystallization of PbI_2, the 2-(4-MSPE)-incorporated perovskite shows weaker absorption intensities (Figure S4a) than that of the control film. It should be ascribed to the coordination effect between 2-(4-MSPE) and $[PbI_6]^{4-}$ as discussed above. Such restraint of the early crystallization of PbI_2 keeps PbI_2 relatively free, which assists the subsequent perovskite nucleation. Upon anti-solvent dripping, the pristine $FAPbI_3$ fails to show distinct absorbance in the 700-800 nm wavelength region, implying that only a small amount of $FAPbI_3$ nuclei is formed during this step. It reflects a slow nucleation rate that is adverse for the deposition of high-quality perovskite films with good coverages.[22] Contrastingly, the absorption peak of 2-(4-MSPE)-treated perovskite instantly shifts to 800 nm (Figure 2e) after anti-solvent pouring, manifesting the efficient and direct nucleation of α phase without the participation of yellow δ phase. To further understand the crystallization dynamics, thermal annealing processes are examined and shown in Figure 2b,d. By summarizing the absorption onset position with annealing time in Figure 2f, the 2-(4-MSPE)-treated film clearly reveals a slower broadening of the absorption spectrum to ~800 nm than that of the pristine one, indicating a retarded crystal growth rate with 2-(4-MSPE) incorporation. In addition, the intensity of the modified film is also higher than that of the control one (Figure S4b), suggesting reduced defects and larger perovskite grains.[23]

The above in-situ absorption spectra show rapid nucleation and slow crystallization for modified perovskite film. Fast nucleation is essential to achieve a high density of heterogeneous nuclei. This ensures a more uniform distribution of perovskite crystals, mitigating the formation of large, dendritic structures detrimental to PSC performance. In contrast, slow crystallization, regulated by supersaturation, allows for the controlled growth of these nuclei, leading to dense, larger and well-covered perovskite crystals. This balance is key to forming high-quality films without defects. The Ostwald ripening mechanism further explains this growth behavior. Smaller particles tend to dissolve more easily due to their higher chemical potential, leading to a concentration gradient that drives solute atoms towards larger particles. This process results in an increase in the average particle size, contributing to a more uniform film structure.[22]In addition, the 'coffee-ring effect' where material accumulates at the edge of a drying droplet, disrupts film uniformity, and prevalent during the initial phase of perovskite film formation, can be mitigated by speeding up nucleation. [24] Consequently, the homogeneity, stacking order, and grains of modified perovskite film are further expected to be distinguished. To verify it, the quality of the resultant perovskite crystals was subsequently evaluated by X-ray diffraction (XRD) patterns. From Figure S5, the XRD intensity ratio between the (100) and (200) facets are determined to be 1.48, 1.92, 1.75, and 1.61 for pristine $FAPbI_3$, 2-(4-MSPE), 2-(3-MSPE) and 2-(2-MSPE) incorporated $FAPbI_3$, respectively, suggesting the dominant crystal growth along (100) lattice plane. Grazing incident wide-angle X-ray scattering (GIWAXS) measurements were further carried out to study the crystallographic orientations, as shown in Figure S6a-d. The scattering ring at q=1.0 Å from 2D GIWAXS patterns of the four perovskite films is assigned to the (100) lattice plane of α-$FAPbI_3$. From the corresponding 1D integrated scattering along the in-plane (IP) and out-of-plane (OOP) directions in Figure S6e-h, the intensity ratio of (100) facet $\frac{I_{OOP}}{I_{IP}}$ increases from 3.52 for control film to 7.96, 6.23, 4.40 for 2-(4-MSPE), 2-(3-MSPE) and 2-(2-MSPE) incorporated films, respectively. It implies that the increased polarity of molecular additives induces a preferred OOP orientation of (100) crystal plane growth, expecting a facilitated charge carrier transport within the α-$FAPbI_3$

polycrystalline thin film.[25] Microstructures of the perovskite lattices were further inspected by high-resolution transmission electron microscope (HRTEM) images, the lattices were analyzed by fast Fourier transform (FFT). It can be seen from Figure 2h that the pristine α-$FAPbI_3$ film exhibits a mixture of (100) and (111) facts corresponding to the lattice spacing of 6.96 Å and 3.82 Å, respectively. The addition of MSPEs reduces the (100) plane spacing to 6.66 Å, 6.89 Å, and 6.94 Å for 2-(4-MSPE), 2-(3-MSPE), and 2-(2-MSPE) respectively, suggesting that higher polarity of MSPE induces a more released residual tensile stress in α-$FAPbI_3$ film. Additionally, 2-(4-MSPE) with the largest dipole moments brings about a high phase purity of (100) planes of the polycrystalline film, which is consistent with the XRD results. Depth-resolved grazing incident XRD (GIXRD) patterns were then conducted to quantitatively analyze the residual stress in the perovskite films, which were recorded at different Ψ ranging from 10° to 50°. From Figure S7, the scattering peaks (2θ) around 32° in the perovskite films experience blue-shifts with the increment of Ψ, indicating the increase of perovskite lattice spacing under residual tensile stresses. Based on the equation $\sigma = -\frac{E}{2(1+v)}\frac{\pi}{180^\circ}\cot\theta_0\frac{\partial(2\theta)}{\partial\sin^2\varphi}$ (where φ, E are the angle of the diffraction vector respective to the sample surface normal and the perovskite modulus, respectively)[26], 2θ-$\sin^2\Psi$ linear function of the films in Figure S8 determines the tensile strains of 39 MPa, 23 MPa, 25 MPa, and 30 MPa for pristine, 2-(4-MSPE)-treated, 2-(3-MSPE)-treated and 2-(2-MSPE)-treated films, respectively. The significantly reduced stresses with MSPE additives are in line with suppressed lattice spacing from HRTEM results. It could be accredited to the rapid nucleation and refined crystallization processes stimulated by the strong interactions of the FAI-2-(4-MSPE)-PbI_2 intermediates with highly polar additives. The released tensile stress predicts higher photovoltaic efficiencies and device stabilities.

Film morphologies of the perovskites were subsequently examined by scanning electron microscope (SEM). The results in Figure 2g demonstrate the elimination of pinholes and defects in the perovskite films with MSPE additions. Additionally, the increment in molecular dipole moment consistently enlarges the perovskite grains with narrower grain size distribution. Cross-sectional SEM images in Figure S9 further demonstrate compact and highly-ordered perovskite grains across the thin film, which could be advantageous to promote charge carrier transport and suppress nonradiative recombination losses. Similarly, atomic force microscope (AFM) images of the four perovskite films in Figure S10 illustrate reduced surface roughness with MSPE additions as compared to that of the control film, which suggests improved interfacial contact between the perovskite film and hole transporting layer (HTL) for better hole extraction.

Distribution of the additive in perovskite film was further analyzed by Time-of-Flight Secondary Ion Mass Spectrometry (ToF-SIMS). By examining the distributions of I^- and SO^{2-} (as shown in Figure S11), it is surprised to observe a higher concentration of SO^{2-} at the upper and lower interfaces of the perovskite layer, with a reduced presence in the middle section. It indicates that the 2-(4-MSPE) is resided dominantly near the top and bottom interfaces, instead of homogeneous distributed in the film as expected. This might be because that majority of the defects and grain boundaries are formed at the bottom [27-29] and upper surface [30-32] of the perovskite films, rather than in the bulk film, during film formation process, as has been previously demonstrated. The larger density of defects and more grain boundaries provides more sites for 2-(4-MSPE) to be interacted with perovskite through hydrogen bond and chelation. In contrast, the bulk layer with less defects and grain boundaries renders the

presentation of 2-(4-MSPE) more challenging due to the limited binding sites. Another possible explanation for this distribution mode is the surface energy differences: additives might migrate preferentially to interfaces due to varying surface energies between the perovskite material and adjacent layers, influencing their final distribution. [33]

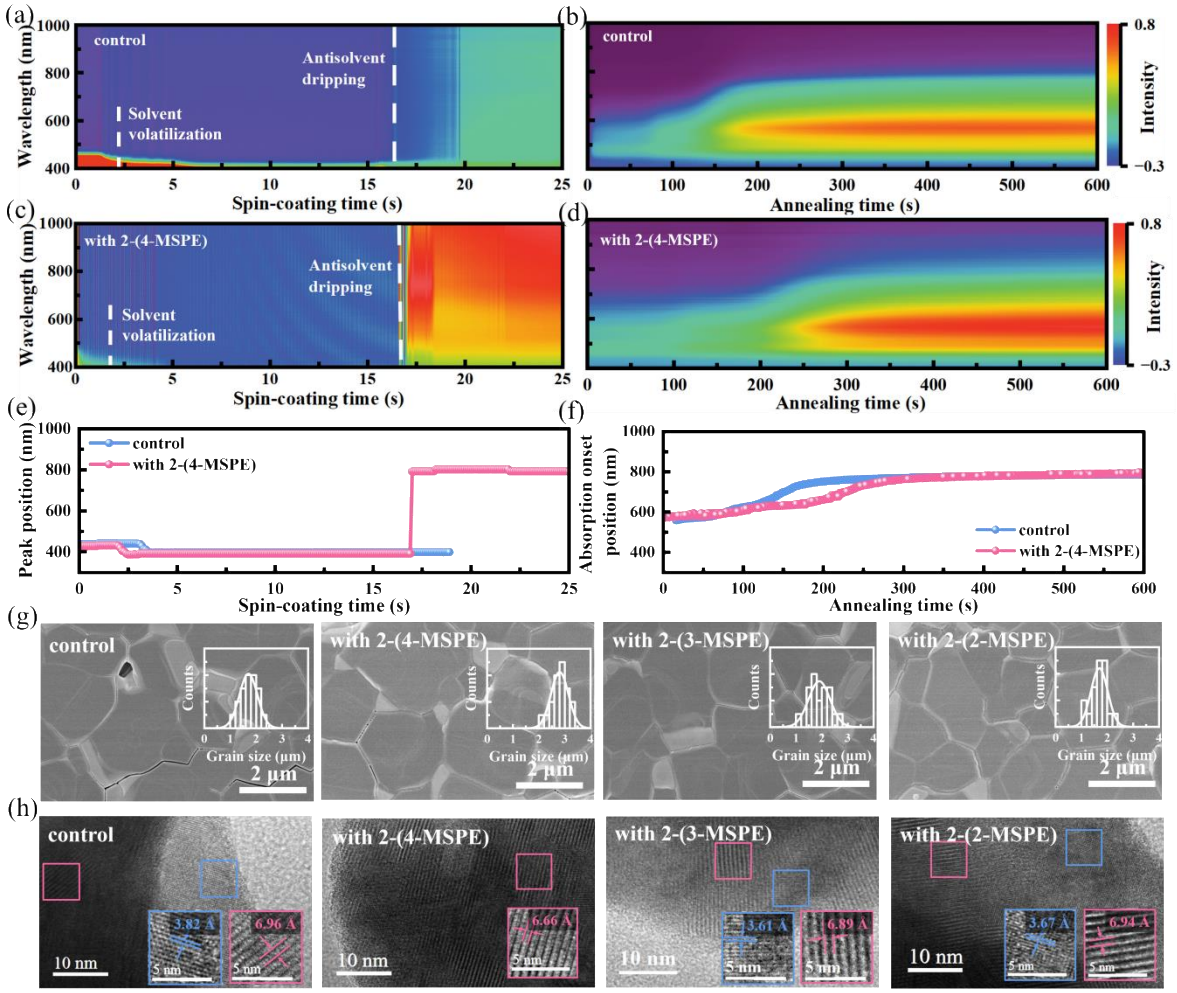

Figure 2. In-situ UV-vis absorption spectroscopy of pristine perovskite film during (a) spin-coating and (b) annealing. In-situ UV-vis absorption spectroscopy of 2-(4-MSPE)-modified perovskite film during (c) spin-coating and (d) annealing. (e) The position of absorption peak during spin-coating. (f) The position of absorption onset during annealing. (g) Scanning electron microscopy (SEM) images of the surface of corresponding perovskite films (the insets are grain size distributions). (h) High-resolution transmission electron microscope (HRTEM) images of corresponding perovskite films.

To dig into the effects of polar additives on the electrical charge distribution of the perovskite films, Kelvin probe force microscopy (KPFM) measurements were conducted to inspect the surface potential of perovskite films (Figure 3a). Contact potential difference (CPD) was recorded by detecting the electrostatic force between the scanning tip and film surface, i.e. $V_{tip} - V_{sample}$.[34] Thus, compared to the film with MSPE additives, the more positive CPD (~ 200 mV) of the control film indicates the more negative surface potential, implying more n-type characteristic of the film surface. It would not only form a large hole transporting barrier but also abet the transportation of electrons at the perovskite/HTL interface. Contrastingly, the addition of MSPE brings about dipole moments and a dielectric environment onto the

perovskite grains, gradually transiting the surface characteristics to less n-type (50 mV for 2-(2-MSPE)) and then more p-type doping (-150 mV for 2-(3-MSPE) and -250 mV for 2-(4-MSPE)) as increasing the polarity of additives. It expects to induce a downward-shifted Fermi level and upward-bended energy alignment at the perovskite/HTL interface, thus eliminating the hole-transporting barrier and increasing the electron migration barrier between perovskite and HTL layer, as shown in Figure S12.[35] Additionally, the MSPE-treated $FAPbI_3$ films demonstrate narrower distributed CPD values, again manifesting an improved uniformity of the perovskite grains.

The exciton dynamics of the perovskite films affected by MSPE additives were further assessed by femtosecond transient absorption spectroscopy (TAS) tested under the excitation pump of 400 nm. The TAS pseudo-color plots of four perovskite films in Figure 3b exhibit negative ground state photobleaching (PB) peaks at ~825 nm, which are assigned to the carrier-filling at the bandage. It is obvious that highly polar 2-(4-MSPE) incorporated film shows stronger PB intensity than those of the control and smaller polar additive treated films, denoting an increased number of photo-excited excitons. Furthermore, from the bi-exponential fitting of the PB decay, an elongated exciton lifetime of the perovskite films from 207.2 ps for control film to 869.6 ps, 475.2 ps, and 426.1 ps for 2-(4-MSPE), 2-(3-MSPE) and 2-(2-MSPE) incorporated films are correspondingly extracted (Figure 3c). The enhanced number of photo-generated excitons and prolonged exciton lifetime predict an improved photovoltaic performance of the devices, which might be ascribed to the refined perovskite crystallization with reduced defect states and lower nonradiative recombination.[36] TAS spectra of the perovskite films are illustrated in Figure S13, from which the full width at half maximum (FWHM) of the PB peaks could be determined to be 64.3 meV, 60.3 meV, 62 meV and 62.7 meV for pristine film, films with 2-(4-MSPE), 2-(3-MSPE), and 2-(2-MSPE), respectively (Figure 3d). The narrower FWHM reflects a reduced number of background carriers originating from the weakening of bandgap oscillations, resulting in the suppression of current leakage in devices.[37]

Steady-state and time-resolved photoluminescence (PL and TRPL) of the perovskite films were tested under the excitation laser pulse of 475 nm, to investigate the recombination dynamics in the films. From the PL spectra in Figure S14a, it is observed that MSPE treatments improve PL quenching of perovskite, The intensified degree also follows the same trend as dipole moment increment, with the most highly polar 2-(4-MSPE) giving the highest PL intensity. Correspondingly, bi-exponentially fitting the TRPL spectra (Figure S14b) affords notably elongated carrier recombination lifetime from 1.27 μs (control) to 2.39 μs (2-(4-MSPE)), 1.74 μs (2-(3-MSPE)), and 1.57 μs (2-(2-MSPE)), respectively, consistent with the PL spectra. Fitting details are illustrated in Table S1. These results evince the suppressed trap-assisted non-radiative recombination in perovskite films with polar molecule addition, which might be explained by two reasons. Firstly, higher dipole moment of MSPE additive results in stronger interactions between the FAI-MSPE hydrogen bonding and PbI_2-MSPE coordination (confirmed by FTIR and XPS results), which induce faster heterogeneous nucleation and retarded crystallization (evidenced by in-situ optical spectra) for refined polycrystalline film morphology with the elimination of defects. Secondly, the dipole moment of molecules could create a dielectric environment to screen the defect capture process, which would be elaborated in the later context. To further examine the photoluminescent properties of the perovskite films

on the microscopic scale, confocal PL mapping of the control and 2-(4-MSPE)-treated films were tested, as shown in Figure 3e,f. It is observed that the polar additive incorporation leads to an improved homogeneity of the photoluminescent characteristics of the perovskite grains, as comparable to the randomly distributed grains with low PL intensities in the control film.

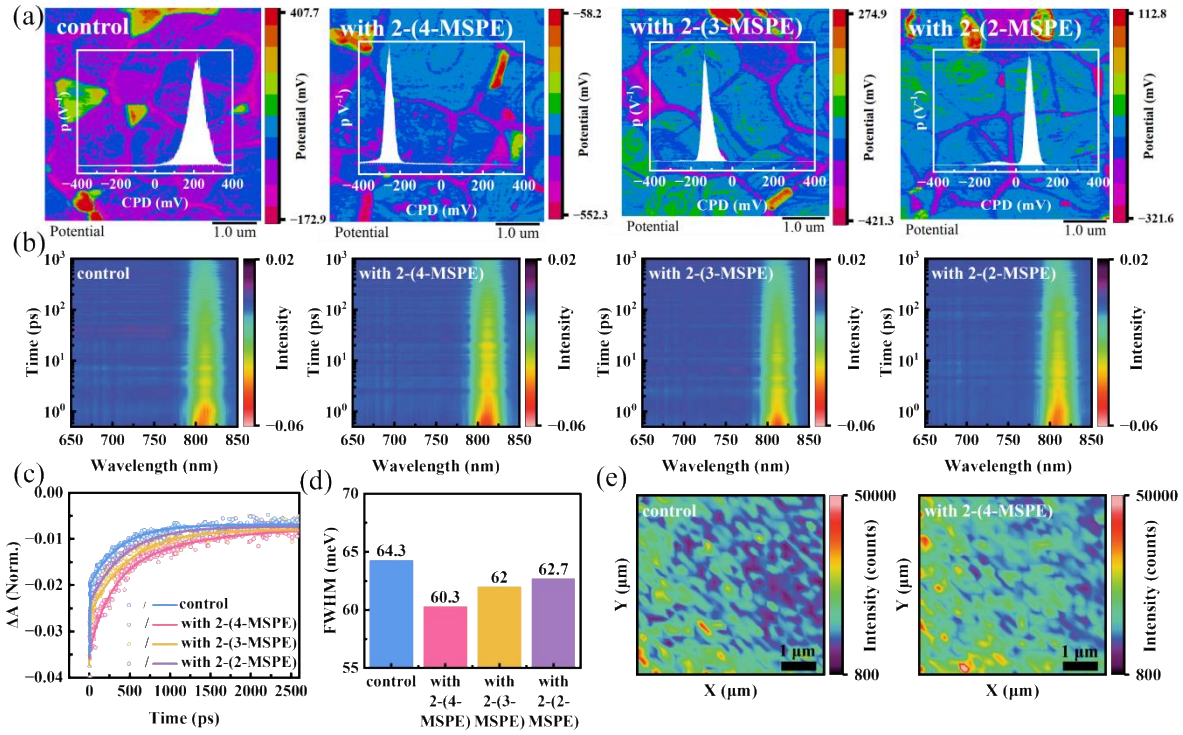

Figure 3. (a) Kelvin probe force microscopy (KPFM) images of corresponding perovskite films (with insets of Contact potential difference (CPD) distribution). (b) Femtosecond transient absorption spectra (TAS) pseudo-color plots of corresponding perovskite films. (c) PB decay curves of perovskite films deduced from TAS. (d) A histogram illustrated full width at half maximum (FWHM) of the photobleaching (PB) peaks of perovskite films. (e) Confocal photoluminescence (PL) mapping of pristine perovskite film and perovskite film with 2-(4-MSPE).

The dielectric response of the perovskite film to polar additives, as well as its effects on the defect capture process, is further studied. Capacitance-frequency (C-F) spectra of the perovskite films were measured to inspect their dielectric characteristics. By comparing the capacitance of the four films in the low-frequency region (<100 Hz, Figure 4a), which arises from the migration of mobile ions in perovskite, the addition of MSPE additives is found to significantly suppress the ion migrations in the film.[38] Consistent with the previous results, 2-(4-MSPE) with the largest dipole moment shows the lowest degree of ion migration, which might be explained by the strong MSPE-FAI hydrogen bonding anchoring I^- mobile ions. This is further supported by the activation energy of ionic migration (E_a^{ion}) of the perovskite films determined from temperature-dependent electrical conductivity measurements (Figure S17). In Figure 4g, an increased E_a^{ion} from 70 meV for the control film to 126 meV for the film with 2-(4-MSPE), 105 meV for the film with 2-(3-MSPE), and 99 meV for the film with 2-(2-MSPE) could be extracted. As light-induced ion migration is acknowledged as the major culprit for light instability of the PSC devices, the suppressed ion migration thus predicts superior operational stability of PSCs.[39] The capacitances at the intermediate frequency region (from 5 x 10^4 to 1 x 10^5 Hz) are then studied to gain a deeper insight into the carrier recombination dynamics since the recombination process generally occurs on hundreds of μs. The dependence

of the dielectric constant on frequency could be plotted according to $\varepsilon_r = \frac{4\pi Ckd}{S}$ (where ε is the dielectric constant, C is the capacitance of devices, k is the electrostatic force constant, d is the thickness, and S is the area of devices), as shown by the inset of Figure 4a. From this equation, the average dielectric constant of 32.77 F/m for the control perovskite, 35.57 F/m for perovskite with 2-(4-MSPE), 35.06 F/m for perovskite with 2-(3-MSPE), and 34.55 F/m for perovskite with 2-(2-MSPE) could be obtained (from 5×10^4 to 1×10^5 Hz). The extracted values (30-40) are in line with other reports for organometallic perovskites[40]. The carrier capture radius (R), which reflects the probability of the carrier escaping from defects, could be further determined by equation $R = \frac{q^2}{4\pi k_b T \varepsilon_0 \varepsilon_r}$.[17] For the control device and devices treated with 2-(4-MSPE), 2-(3-MSPE), and 2-(2-MSPE), the carrier capture radii are determined to be 1.71 nm, 1.57 nm, 1.60 nm, and 1.62 nm, respectively. The larger dielectric constants of MSPE-treated perovskite films suggest smaller R and smaller defect capture cross-section than that of the control film, thus lowering the chances of carriers being captured by trap states. In light of these findings, we have developed a mechanism to elucidate dielectric screening when MSPE is introduced. In untreated perovskite films, most defects, such as lead vacancies (as indicated in Figure S15a) and iodide dangling bonds, are predominantly located at grain boundaries. The incorporation of MSPE into these grain boundaries leads to the O=S=O groups in MSPE molecules potentially occupying the charged lead vacancies, thus attenuating the electrostatic interaction between defects and holes as shown in Figure 4j. In a similar way, the -NH_2 groups interacting with iodide dangling bonds, thereby weakening the electrostatic interaction between defects and electrons. In addition, the changes in the intermediate frequency region (from 5×10^4 to 1×10^5 Hz) corroborate the enhancement in dielectric properties due to MSPE. This adjustment in space-charge distribution, resulting from the addition of MSPE, is believed to significantly diminish the defect capture cross-section as delineated above (see Figure 4j). Such dielectric screening can effectively reduce the impact of charged defects, essentially rendering them 'undetectable' to charge carriers. This phenomenon, referred to as 'defect stealth', is advantageous for enhancing the movement of charge carriers within the films.

To quantitatively analyze the density of deep-level trap states of the perovskite films, thermal admittance spectroscopy was further conducted. The temperature-dependent C-F spectra are shown in Figure S16a-d, illustrating the spectral shift to a higher frequency with increasing temperature. It should be related to the time constant of carrier de-trapping from the defect states under different temperatures. The defect activation energy (E_a^{defect}) determined from Figure 4b is reduced from 0.46 eV (control film) to 0.23 eV (2-(4-MSPE)-treated film), 0.30 eV (2-(3-MSPE)-treated film) and 0.25 eV (2-(2-MSPE)-treated film), respectively, which indicates a lower probability of forming defects in highly polar MSPE-treated perovskite. The energetic defect distribution (t-DOS) of the films can be further derived according to the method described in SI. In Figure 4c, the MSPE treatment sequentially lowers the energy level of trap states from 0.26 eV to 0.17 eV with increasing MSPE dipole moment. The deep defect state around 0.10 eV - 0.25 eV should be assigned to iodine interstitials according to previous DFT calculations,[41] which is defined as the only low-energy deep traps and non-radiative recombination centers among the intrinsic point defects. The density of trap states is also substantially reduced according to t-DOS spectra. These results, together with the previous PL and TRPL spectra, evince that the suppressed non-radiative recombination might majorly

originate from the reduced iodine interstitial migrations through hydrogen bonding and dielectric screening effects, excluding the significant contributions from the chemical passivation of the sulfonyl group on lead vacancies.

With the reduced carrier capture process by charge defects, the phonon scattering process is expected to be suppressed as well. In organometallic halide perovskite, the electron-phonon coupling is dominated by the Fröhlich interactions between the longitudinal optical (LO) phonons and electrons. According to Bose-Einstein thermal distribution $\Gamma(T) = \Gamma_0 + \Gamma_{LO}(T) = \Gamma_0 + \frac{\Upsilon_{LO}}{e^{E_{LO}/kT}-1}$ (Γ_0 is the inhomogeneous broadening unrelated to the temperature, Γ_{LO} indicates the homogeneous broadening), the temperature-related broadening of PL spectra is caused by the interactions of LO phonons and electrons.[42] Therefore, temperature-dependent (100 K-200 K) PL spectra were measured and illustrated in Figure 4d,e. Based on the dependence of FWHM of the PL spectra on various temperatures, the coupling strength γ_{LO} can be extracted to be 440 meV and 110 meV for control and 2-(4-MSPE)-treated films (Figure 4f). The reduced coupling between LO phonon and electron further testifies to the lower phonon scattering effects, which implies suppressed non-radiative recombination.[43]

I-V characteristics in Figure 4k,l tested the trap density and carrier mobility of the perovskite films based on the space-charge-limited current (SCLC) model. Trap densities and carrier mobilities of the control and target films can be calculated according to the method described in SI. From the values summarized in Table S2-3, the decreased trap density of polar additive treated films could be ascribed to the refined perovskite crystal quality with the elimination of defects.[44] The remarkably improved carrier mobilities with MSPE treatment might be explained by the phase-pure and preferred orientation of (100) facet along vertical direction relative to substrate induced by highly polar MPSE (evidenced by TEM, XRD, and GIWAXS results). To investigate the charge recombination dynamics on the device level, electrochemical impedance spectroscopy (EIS) of the PSCs under an external voltage of 0.1-0.9 V was measured and shown in Figure 4h and Figure S18. Figure 4h compares the EIS under 0.9 V, which reveals enhanced recombination resistance of the MSPE-treated device over that of the control one. From Figure S18, carrier recombination lifetimes of the perovskite films could be extracted and summarized in Figure 4i. It is observed that the polar additives lead to successively prolonged carrier recombination lifetimes with increasing polarity. These results evidence suppressed non-radiative recombination in MPSE-treated films. Charge recombination processes in devices were further studied by light intensity (P_{light}) dependent J_{SC} and V_{OC}. From Figure S20, slopes of V_{OC} dependence on light intensity (P_{light}) are found to be 1.82, 1.47, 1.51, and 1.62 kT/q for control, 2-(4-MSPE), 2-(3-MSPE), and 2-(2-MSPE)-treated devices, respectively. A suppression of trap-assisted recombination in the MSPE-treated devices could be concluded by the less deviation of the slope from kT/q. Furthermore, the dependence of J_{SC} on P_{light} shows slope values of 0.87, 0.98, 0.97, and 0.88 for control, 2-(4-MSPE), 2-(3-MSPE), and 2-(2-MSPE)-treated devices (Figure S20), respectively, implying decreased monomolecular recombination in target devices. Additionally, the Mott-Schottky curves and descendant results are enumerated in Figure S21 and Table S4. The built-in potential V_{bi} of PSCs is increased from 0.98 V for a pristine device to 1.06 V, 1.05 V, and 1.04 V for 2-(4-MSPE), 2-(3-MSPE), and 2-(2-MSPE)-treated devices, respectively, due to the reduced trap-assisted recombination losses, predicting a higher open-circuit voltage (V_{OC}).[45] The charge density N_d is lessened from $7.69 \times 10^{15}\ cm^{-3}$ for a pristine device to $5.07 \times 10^{15}\ cm^{-3}$,

$5.30 \times 10^{15}\ cm^{-3}$, and $5.67 \times 10^{15}\ cm^{-3}$ for 2-(4-MSPE), 2-(3-MSPE), and 2-(2-MSPE)-treated devices, respectively, indicating fewer charge accumulation at interfaces[46] in accord with the KPFM results. Furthermore, MSPE additives lead to an increase of the depletion width from 81 nm (without additives) to 104 nm (with 2-(4-MSPE)), 101 nm (with 2-(4-MSPE)), and 98 nm (with 2-(4-MSPE)) which benefits to accelerate hole transportation and reduce charge carrier recombination.[47]

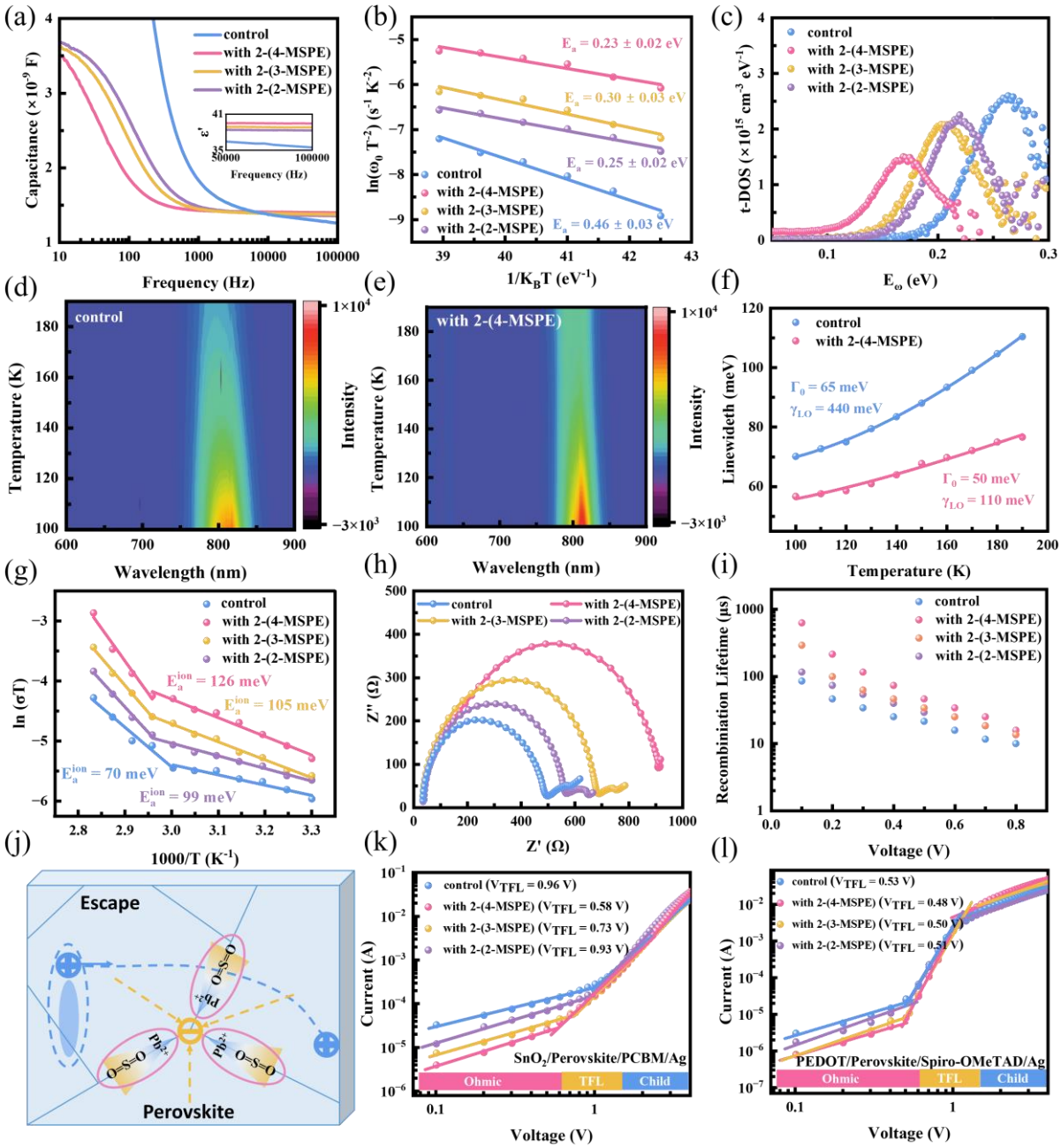

Figure 4. (a) Capacitance-frequency (C-F) spectra of devices (the inset is the dielectric constant-frequency plot). (b) The Arrhenius plots of the attempt-to-escape frequencies to extract the defect activation energy (E_a) for PSCs. (c) Trap density of states (t-DOS) deduced from temperature-dependent C-F curves of PSCs. Pseudo-color mapping of temperature-dependent PL spectra of (d) pristine perovskite film and (e) perovskite films with 2-(4-MSPE) from 100 K to 200 K. (f) full width at half maximum (FWHM) of the PL peaks vs. temperature plot of perovskite films. (g) temperature-dependent conductivity of perovskite films. (h) Nyquist plots of PSCs at 0.9 V with a frequency range between 1MHz and 1 Hz. (i) Recombination lifetime of devices under different biases

derived from the Nyquist plots in Figure S18. (j) Schematic diagram of carrier escape in perovskite films. Space-charge-limited current (SCLC) analysis of (k) electron-only devices and (l) hole-only devices.

Based on the above characterizations, the polar additives are evidenced to trigger an improved crystallization in terms of preferred (100) crystal growth, enlarged grain size, and high phase purity, as well as the dielectric screening of the carrier capture process for reduced non-radiative recombination. Their effects on photovoltaic performances were subsequently scrutinized by PSCs with a device architecture of ITO/SnO_2/perovskite/ Spiro-OMeTAD/Ag (Figure S22). The J-V characteristics were recorded under simulated one sun illumination at an intensity of 100 mW cm^{-2} (AM 1.5 spectrum). The optimal concentration of MSPE was firstly studied, and 2-(4-MSPE)-treated PSCs were tested as an example. Based on J-V characteristics at different 2-(4-MSPE) concentrations, the photovoltaic performances can be summarized in Figure S23 and Table S5, from which the optimal concentration is determined to be 0.19 mg/mL. Supporting evidence is also demonstrated in the SEM images of perovskite films with different 2-(4-MSPE) concentrations (Figure S24). Films with a 2-(4-MSPE) concentration below 0.19 mg/mL exhibited cracks and holes, while those bove 0.19 mg/mL led to a decrease in crystal grain sizes. J-V characteristics of the champion cells of control and MSPE-treated PSCs are compared in Figure 5a, forward and reverse scanned J-V curves are shown in Figure S25, and the photovoltaic parameters are summarized in Table S6. Evidently, MSPE-treated PSCs demonstrate significantly increased PCE from 22.9% to 25.2% (with 2-(4-MSPE)), 24.3% (with 2-(3-MSPE)), and 23.6% (with 2-(2-MSPE)), respectively, with simultaneously increased V_{OC}, J_{SC}, and FF. The improved photovoltaic performances could be accredited to both improved perovskite crystallization with preferred crystallographic orientation and suppressed non-radiative recombination by dielectric screening. The former majorly contributes to facilitated carrier transporting properties and reduced leaking current, resulting in J_{SC} and FF increment. While the latter renders the significant V_{OC} enhancement. From Figure 5b, steady-state PCEs of the PSCs are observed to be 21.3% and 24.3% for control and 2-(4-MSPE) treated devices, respectively from the steady-state PCE output (SPO) tracking, attesting the accuracy of J-V results. Integration of the external quantum efficiency (EQE) spectra of PSCs (Figure S26) affords J_{SC} of 24.79 mA cm^{-2} and 24.09 mA cm^{-2} for control and target devices, respectively, also consistent with J-V characteristics. From statistical PCE in Figure 5c, where performances of 50 individual devices were recorded, polar MSPE incorporated PSCs demonstrate good reproducibility due to improved polycrystalline film morphology and homogeneity.

To have an in-depth understanding of the V_{OC} enhancement of PSCs with polar molecular additives, energy loss E_{loss} of the control and target devices were studied by electroluminescence (EL) and highly sensitive EQE. From the equation $E_{loss} = \Delta E_1 + \Delta E_2 + \Delta E_3 = E_g - eV_{OC}$, where e is the charge of an electron, E_g is the optical bandgap of the perovskite, ΔE_1 *and* ΔE_2 are the radiative recombination above and below the bandgap, and ΔE_3, also known as $E_{loss\,nr}$, is the non-radiative recombination loss. It can be derived that by minimizing the ΔE_3, V_{OC} would be improved. Figure 5d shows that EQE_{EL}% of control, 2-(4-MSPE)-treated, 2-(3-MSPE)-treated, and 2-(2-MSPE)-treated device is -5.23, -3.45, -4.26, and -4.53. By calculating $\Delta E_3 = -kTln(EQE_{EL})$,[48] it is found that ΔE_3 of the device is weakened from 0.133 (without additive) to 0.088 (with 2-(4-MSPE)), 0.108 (with 2-(3-MSPE)), and 0.115

(with 2-(2-MSPE)), which indicates that the non-radiative recombination is suppressed by more polar MSPEs. It is in accordance with the previous discussion and the V_{OC} trend.

MSPE additives affecting the intrinsic and operational long-term stabilities of PSCs were then inspected. The structural stability of $FAPbI_3$ perovskite was investigated by recording the efficiency evolution of 50 unencapsulated devices under controlled relative humidity (RH) of ~40% in ambient air, as illustrated in Figure 5e. The 2-(4-MSPE)-treated PSCs show notably improved long-term stability with over 94% of the initial PCE retained after 2000 hours of aging. It could be attributed to the released residual tensile stresses in α-$FAPbI_3$ film due to improved film and crystal quality. Figure 5f compares the operational stability of control and 2-(4-MSPE)-treated PSCs, which was tested by tracking the maximum power point (MPP) under 1 sun illumination in the N_2 environment. From Figure 5f, the target PSCs demonstrate significantly improved operational stability with over 93% of the initial PCE maintained after 450 hours of continuous illumination, while that of the control device shows rapid degradation with only 69% of the original PCE retained. This could be explained by the restrained iodide ion migrations thanks to the strong FAI-2-(4-MSPE) hydrogen bonding, as previously evidenced by temperature-dependent conductivity measurements.

In an attempt to prove the viability of a highly polar additive strategy towards the scalable fabrication of PSCs, large-area PSMs (active area of 70 cm^2) were developed using pristine and 2-(4-MSPE)-incorporated $FAPbI_3$ films. As schematically illustrated in Figure 5g, the module consists of 18 series-connected sub-cells. From the I-V and P-V characteristics shown in Figure 5h and Figure S27, the target device demonstrates a drastically improved photovoltaic performance of the solar modules, with an impressive PCE of 20.5%, V_{OC} of 20.71 V, I_{SC} of 1.34 mA cm^{-2}, FF of 73.54% and power of 1.43 W. In comparison, the control PSMs show an inferior PCE of 16.5%, with V_{OC} of 20.17 V, I_{SC} of 1.31 mA cm^{-2}, FF of 61.94% and power of 1.15 W (Table S7). Noted that this is one of the highest reported PCEs for solar modules with over 70 cm^2 device area. Statistical PCE of the solar modules are summarized in Figure 5i, presenting improved reproducibility of the 2-(4-MSPE)-treated PSMs over that of the control ones. As a result, the incorporation of highly polar additive, which delivers homogeneous and high-quality perovskite film morphology through controllable nucleation and crystallization steps, is manifested to be an effective and feasible route to scalable deposition of perovskite thin films and solar modules.

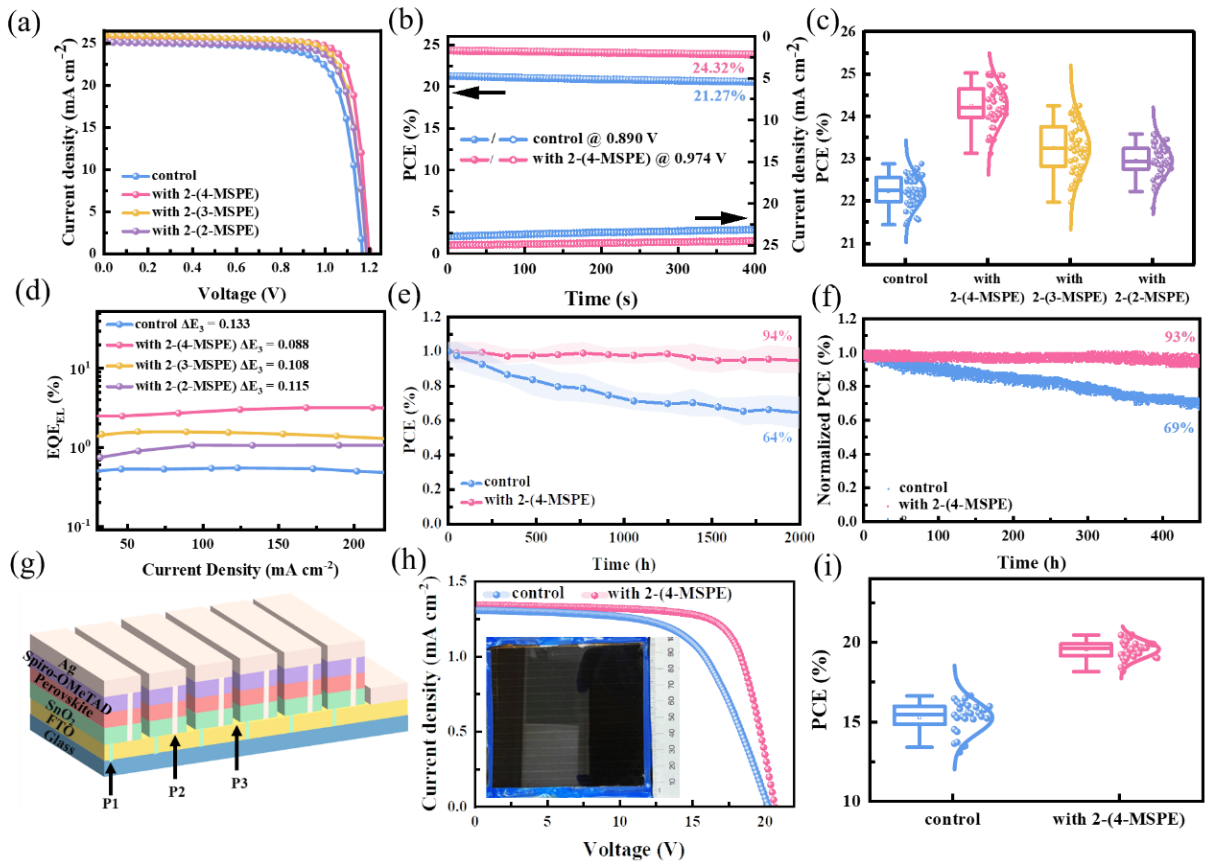

Figure 5. (a) J-V curves of champion PSCs. (b) Stabilized power output (SPO) and steady-state current density of devices without additive and with 2-(4-MSPE) under working conditions with 100 mW cm^{-2} irradiation. (c) PCE normal distribution of PSCs. (d) EQE_{EL} versus current density of devices. (e) Long-term stability test of pristine devices and devices with 2-(4-MSPE) under relative humidity (RH) of ~40% in ambient air. (f) Maximum power point (MPP) tracking of control devices and devices with 2-(4-MSPE) under 1 sun illumination in the N_2 environment. (g) Schematic illustration of large-area perovskite solar modules (PSMs) based on the structure of Glass/FTO/SnO_2/Perovskite/Spiro-OMeTAD/Ag. (h) J-V curves of champion PSMs without additive (control) and with 2-(4-MSPE) (with an inset of PSMs picture). (i) PCE normal distributions of the PSMs without additive (control) and with 2-(4-MSPE).

Conclusions

In summary, the effects of different polarities of molecular additives (MSPE) on perovskite crystallization dynamics and dielectric screening in the carrier capture process are also systematically studied in this work. Stronger MSPE-$FAPbI_3$ interactions, in terms of MSPE-FAI hydrogen bonding and MSPE-PbI_2 coordination, are obtained by larger dipole moment of 2-(4-MSPE), which triggers a rapid and direct nucleation of α-$FAPbI_3$ without the participation of yellow δ-phase. It assists in the formation of improved perovskite film quality with preferred (100) orientation and suppressed defects. Additionally, highly polar 2-(4-MSPE) endows the perovskite grains with a dielectric environment, which effectively screens the electron capture pathways and reduces the nonradiative recombination losses. In view of the combined functions of dipole additives, PSCs with 2-(4-MSPE) treatment deliver an impressive PCE of 25.2%, the device also shows remarkable ambient and operational long-term stabilities. By further extending the strategy to scalable deposition, an exceptional PCE of 20.5% has been achieved by large-area PSM (active area 70 cm^2), which is one of the highest reported efficiencies for such area solar modules. These findings are pivotal in guiding future research towards the

exploration of molecular structures with high dipole moments and strong coordination capabilities, a direction that holds promise for further advancements in PSCs. It is believed that the design of molecular additives for PSCs is a multifaceted process, necessitating careful consideration of polarity, hydrogen bonding, and chelation effects, which are all critical factors to optimize the performance and stability of PSCs and PSMs.

ACKNOWLEDGMENTS

This work is financially supported by the National Natural Science Foundation of China (U21A20331, 81903743, 22279151, and 22275004) and the National Science Fund for Distinguished Young Scholars (21925506). The unfunded collaborative work of H.W. and K.W. is supported by the International Institute of Biosensing (IIB), headquartered at Penn State University.

AUTHOR CONTRIBUTIONS

R.T. designed the experiments, fabricated the perovskite films and devices, and analyzed measured results. C.L. conceived the idea and guided the work. Y.M., Y.W., R.C., J.Z., H.W., X.L. helped the characterizations; S.Y. calculated the dipole moment; K.S. calculated the adsorption energy; C.L., Z.G., B.T., D.W., H.D., and K.W. helped to revise the manuscript. All authors commented on this paper.

DECLARATION OF INTERESTS

The authors declare no competing interests.

References

[1] M. M. Lee, J. Teuscher, T. Miyasaka, T. N. Murakami, H. J. Snaith, *Science* **2012**, *338*, 643.

[2] W. S. Yang, J. H. Noh, N. J. Jeon, Y. C. Kim, S. Ryu, J. Seo, S. Il Seok, *Science* **2015**, *348*, 1234.

[3] D. Luo, W. Yang, Z. Wang, A. Sadhanala, Q. Hu, R. Su, R. Shivanna, G. F. Trindade, J. F. Watts, Z. Xu, T. Liu, K. Chen, F. Ye, P. Wu, L. Zhao, J. Wu, Y. Tu, Y. Zhang, X. Yang, W. Zhang, R. H. Friend, Q. Gong, H. J. Snaith, R. Zhu, *Science* **2018**, *360*, 1442.

[4] Y. Zheng, R. Su, Z. Xu, D. Luo, H. Dong, B. Jiao, Z. Wu, Q. Gong, R. Zhu, *Sci. Bull.* **2019**, *64*, 1255.

[5] H. Kanda, V. Dan Mihailetchi, M. Gueunier-Farret, J. Kleider, Z. Djebbour, J. Alvarez, B. Philippe, O. Isabella, M. R. Vogt, R. Santbergen, P. Schulz, F. Peter, M. K. Nazeeruddin, J. P. Connolly, *Interdisciplinary Materials* **2022**, 1, 148.

[6] Y. Mo, C. Wang, X. Zheng, P. Zhou, J. Li, X. Yu, K. Yang, X. Deng, H. Park, F. Huang, Y. Cheng, *Interdisciplinary Materials* **2022**, 1, 309.

[7] National Renewable Energy Laboratory (NREL), *Photovoltaic Research, Best Research-Cell Efficiency Chart*, **2023**, https://www.nrel.gov/pv/cell-efficiency.html.

[8] W.-C. Qiao, J.-Q. Liang, W. Dong, K. Ma, X. L. Wang, Y.-F. Yao, *NPG Asia. Mater.* **2022**, *14*, 49.

[9] W. Hui, L. Chao, H. Lu, F. Xia, Q. Wei, Z. Su, T. Niu, L. Tao, B. Du, D. Li, Y. Wang, H. Dong, S. Zuo, B. Li, W. Shi, X. Ran, P. Li, H. Zhang, Z. Wu, C. Ran, L. Song, G. Xing, X. Gao, J. Zhang, Y. Xia, Y. Chen, W. Huang, *Science* **2021**, *371*, 1359.

[10] H. Liu, N. Li, Z. Chen, S. Tao, C. Li, L. Jiang, X. Niu, Q. Chen, F. Wang, Y. Zhang, Z. Huang, T. Song, H. Zhou, *Adv. Mater.* **2022**, *34*, 2204458.
[11] T. Bu, J. Li, H. Li, C. Tian, J. Su, G. Tong, L. K. Ono, C. Wang, Z. Lin, N. Chai, X.-L. Zhang, J. Chang, J. Lu, J. Zhong, W. Huang, Y. Qi, Y.-B. Cheng, F. Huang, *Science* **2021**, *372*, 1327.
[12] L. Yin, W. Huang, J. Fang, Z. Ding, C. Jin, Y. Du, L. Lang, T. Yang, S. Wang, W. Cai, C. Liu, G. Zhao, Y. Yang, S. (Frank) Liu, T. Bu, K. Zhao, *Advanced Materials* **2023**, 2303384.
[13] Y. Jiang, J. Wang, H. Zai, D. Ni, J. Wang, P. Xue, N. Li, B. Jia, H. Lu, Y. Zhang, F. Wang, Z. Guo, Z. Bi, H. Xie, Q. Wang, W. Ma, Y. Tu, H. Zhou, X. Zhan, *J. Am. Chem. Soc.* **2022**, *144*, 5400.
[14] F. Wang, S. Bai, W. Tress, A. Hagfeldt, F. Gao, *npj Flex. Electron.* **2018**, *2*, 22.
[15] M. Saba, M. Cadelano, D. Marongiu, F. Chen, V. Sarritzu, N. Sestu, C. Figus, M. Aresti, R. Piras, A. Geddo Lehmann, C. Cannas, A. Musinu, F. Quochi, A. Mura, G. Bongiovanni, *Nat. Commun.* **2014**, *5*, 5049.
[16] R. Su, Z. Xu, J. Wu, D. Luo, Q. Hu, W. Yang, X. Yang, R. Zhang, H. Yu, T. P. Russell, Q. Gong, W. Zhang, R. Zhu, *Nat. Commun.* **2021**, *12*, 2479.
[17] J. Zhang, B. Che, W. Zhao, Y. Fang, R. Han, Y. Yang, J. Liu, T. Yang, T. Chen, N. Yuan, J. Ding, S. (Frank) Liu, *Adv. Mater.* **2022**, *34*, 2202735
[18] [1]J. S. Kim, T.-W. Lee, *Light: Science & Applications* **2023**, *12*, 232.
[19] Y. Sun, L. Ge, L. Dai, C. Cho, J. Ferrer Orri, K. Ji, S. J. Zelewski, Y. Liu, A. J. Mirabelli, Y. Zhang, J.-Y. Huang, Y. Wang, K. Gong, M. C. Lai, L. Zhang, D. Yang, J. Lin, E. M. Tennyson, C. Ducati, S. D. Stranks, L.-S. Cui, N. C. Greenham, *Nature* **2023**, *615*, 830.
[20] A. Priyadarshi, L. J. Haur, P. Murray, D. Fu, S. Kulkarni, G. Xing, T. C. Sum, N. Mathews, S. G. Mhaisalkar, *Energy Environ. Sci.* **2016**, *9*, 3687.
[21] Y. Hou, H. Wu, J. Yoon, L. Zheng, D. Yang, T. Ye, K. Wang, K. Wang, S. Priya, *Adv. Energy Mater.* **2023**, *13*, 202300570.
[22] C. Liu, Y.-B. Cheng, Z. Ge, *Chem. Soc. Rev.* **2020**, *49*, 1653.
[23] T. Yang, C. Ma, W. Cai, S. Wang, Y. Wu, J. Feng, N. Wu, H. Li, W. Huang, Z. Ding, L. Gao, S. (Frank) Liu, K. Zhao, *Joule* **2023**, *7*, 574.
[24] Q. Zhang, H. Liu, X. Tan, H. Wang, Y. Song, X. Wei, Y. Deng, W. Li, L. Zhu, Z. Cui, Y. Bai, H. Chen, *Chem. Eng. J.* **2023**, *454*, 140147.
[25] G. Kim, H. Min, K. S. Lee, D. Y. Lee, S. M. Yoon, S. Il Seok, *Science* **2020**, *370*, 108.
[26] C. Zhu, X. Niu, Y. Fu, N. Li, C. Hu, Y. Chen, X. He, G. Na, P. Liu, H. Zai, Y. Ge, Y. Lu, X. Ke, Y. Bai, S. Yang, P. Chen, Y. Li, M. Sui, L. Zhang, H. Zhou, Q. Chen, *Nat. Commun.* **2019**, *10*, 815.
[27] S.Chen, X. Dai, S. Xu, H. Jiao, L. Zhao, J. Huang, *Science* **2021**, 373, 902.
[28] X. Yang, D. Luo, Y. Xiang, L. Zhao, M. Anaya, Y. Shen, J. Wu, W. Yang, Y. H. Chiang, Y. Tu, R. Su, Q. Hu, H. Yu, G. Shao, W. Huang, T. P. Russell, Q. Gong, S. D. Stranks, W. Zhang, R. Zhu, *Adv. Mater.* **2021**, 33.
[29] Z. Zheng, F. Li, J. Gong, Y. Ma, J. Gu, X. Liu, S. Chen, M. Liu, *Adv. Mater.* **2022**, 34.
[30] C. Liu, Y. Yang, H. Chen, J. Xu, A. Liu, A. S. R. Bati, H. Zhu, L. Grater, S. S. Hadke, C. Huang, V. K. Sangwan, T. Cai, D. Shin, L. X. Chen, M. C. Hersam, C. A. Mirkin, B. Chen, M. G. Kanatzidis, E. H. Sargent, *Science* **2023**, 382, 810.
[31] M. Degani, Q. An, M. Albaladejo-Siguan, Y. J. Hofstetter, C. Cho, F. Paulus, G. Grancini, Y. Vaynzof, *Sci. Adv.* **2021**, 7.
[32] X. Li, Z. Ying, J. Zheng, X. Wang, Y. Chen, M. Wu, C. Xiao, J. Sun, C. Shou, Z. Yang, Y. Zeng, X. Yang, J. Ye, *Adv. Mater.* **2023**, 35.
[33] M. Vasilopoulou, A. Fakharuddin, A. G. Coutsolelos, P. Falaras, P. Argitis, A. R. b. M. Yusoff, M. K. Nazeeruddin, *Chem. Soc. Rev.* **2020**, 49, 4496.

[34] S. Tan, T. Huang, I. Yavuz, R. Wang, T. W. Yoon, M. Xu, Q. Xing, K. Park, D.-K. Lee, C.-H. Chen, R. Zheng, T. Yoon, Y. Zhao, H.-C. Wang, D. Meng, J. Xue, Y. J. Song, X. Pan, N.-G. Park, J.-W. Lee, Y. Yang, *Nature* **2022**, *605*, 268.
[35] C. Luo, G. Zheng, F. Gao, X. Wang, C. Zhan, X. Gao, Q. Zhao, *Nat. Photonics* **2023**.
[36] J. Li, L. Xie, Z. Pu, C. Liu, M. Yang, Y. Meng, B. Han, S. Bu, Y. Wang, X. Zhang, T. Wang, Z. Ge, *Adv. Funct. Mater.* **2023**, *33*, 202301956.
[37] L. Xie, J. Liu, J. Li, C. Liu, Z. Pu, P. Xu, Y. Wang, Y. Meng, M. Yang, Z. Ge, *Adv. Mater.* **2023**, 202302752.
[38] X. Li, Z. Ying, J. Zheng, X. Wang, Y. Chen, M. Wu, C. Xiao, J. Sun, C. Shou, Z. Yang, Y. Zeng, X. Yang, J. Ye, *Adv. Mater.* **2023**, *35*, 202211962.
[39] C. Ma, M.-C. Kang, S.-H. Lee, S. J. Kwon, H.-W. Cha, C.-W. Yang, N.-G. Park, *Joule* **2022**, *6*, 2626.
[40] T.-Y. Yang, G. Gregori, N. Pellet, M. Grätzel, J. Maier, *Angew.* **2015**, *54*, 7905.
[41] H.-S. Duan, H. Zhou, Q. Chen, P. Sun, S. Luo, T.-B. Song, B. Bob, Y. Yang, *Phys. Chem. Chem. Phys.* **2015**, *17*, 112.
[42] J. Yan, W. Zhang, S. Geng, C. Qiu, Y. Chu, R. Meng, P. Zeng, M. Liu, Z. Xiao, Y. Hu, *Chem. Mater.* **2023**, *35*, 289.
[43] Q. Wei, J. Yin, O. M. Bakr, Z. Wang, C. Wang, O. F. Mohammed, M. Li, G. Xing, *Angew.* **2021**, *133*, 11052.
[44] Y. Meng, C. Liu, R. Cao, J. Zhang, L. Xie, M. Yang, L. Xie, Y. Wang, X. Yin, C. Liu, Z. Ge, *Adv. Funct. Mater.* **2023**, *33*, 202214788.
[45] B. Han, Y. Wang, C. Liu, K. Sun, M. Yang, L. Xie, S. Yang, Y. Meng, S. Lin, P. Xu, J. Li, Q. Qiu, Z. Ge, *Angew.* **2023**, *62*, 202217526.
[46] K. Zheng, J. Ge, C. Liu, Q. Lou, X. Chen, Y. Meng, X. Yin, S. Bu, C. Liu, Z. Ge, *InfoMat.* **2021**, *3*, 1431.
[47] S. Ye, H. Rao, Z. Zhao, L. Zhang, H. Bao, W. Sun, Y. Li, F. Gu, J. Wang, Z. Liu, Z. Bian, C. Huang, *J. Am. Chem. Soc.* **2017**, *139*, 7504.
[48] D. Luo, R. Su, W. Zhang, Q. Gong, R. Zhu, *Nat. Rev. Mater.* **2019**, *5*, 44.